International Communications in Heat and Mass Transfer 157 (2024) 107741

Contents lists available at ScienceDirect

International Communications in Heat and Mass Transfer

journal homepage: www.elsevier.com/locate/ichmt

Enhancing PCM thermal management in multi-cycle melting-solidification

D. Dubert [a], B. Šeta [b,*], J. Massons [a], Jna. Gavaldà [a], M.M. Bou-Ali [c], X. Ruiz [a], V. Shevtsova [c,d]

[a] Universitat Rovira i Virgili, Tarragona 43003, Spain
[b] Dept. of Civil and Mech. Engineering, Technical University of Denmark, Produktionstorvet, Lyngby 2800, Denmark
[c] Fluid Mechanics Group, Faculty of Engineering, Mondragon University, Loramendi 4, Mondragon 20500, Spain
[d] IKERBASQUE, Basque Foundation for Science, Bilbao 20500, Spain

ARTICLE INFO

Keywords:
Phase change material
Melting/solidification cycle
Marangoni
Heat transfer
Microgravity

ABSTRACT

We present a comprehensive study on heat transfer in phase-change materials (PCMs), focusing on both melting and solidification phases, different temperature scenarios, an assessment of practical implementation aspects, and Marangoni convection. The research examines heat transfer rates during the melting-solidification cycle, with a focus on gallium (*Ga*) and n-eicosane (C20), the latter being a candidate for the MarPCM project aboard the ISS [1]. The paper explores different temperature scenarios using *Ga* to optimize PCM performance. N-eicosane requires extensive computational resources due to its significant thermal time, whereas gallium allows for more efficient simulations. The most effective scenario involves switching temperatures between cold and hot walls at a certain moment, which occurs earlier than the full melting time or reaching steady state. This specific moment corresponds to the beginning of a decrease in heat extraction efficiency. The success of this scenario relies on the symmetric thermal boundary conditions and multi-cyclic temperature inversion. We suggest that the implementation of this scenario is similar to rotating the PCM body within its package while maintaining the temperature of the external walls constant. Extending the strategy to n-eicosane yields promising results. This study also highlights the importance of Marangoni convection in heat transfer mechanisms.

1. Introduction

Phase change materials have the ability to absorb and release heat during the phase transition (solid to liquid and vice versa), providing a passive thermal control mechanism. This can be advantageous in space applications where managing temperature fluctuations is crucial. Since the 1970s, solid Phase Change Material (PCM) systems have played an important role in various space missions, particularly within the Venera Soviet Missions to Venus (Venera 8, 9, and 10). The PCM systems have been employed as a part of spacecraft thermal control [2] and as stabilizing protective shields against diurnal thermal variations in environments such as the Moon and Mars. Noteworthy examples include their use in the Lunar Roving Vehicle during the Apollo 15 mission and in Mars rovers such as Sojourner, Spirit, Opportunity, Curiosity, and Perseverance [3,4]. Nowadays, PCM systems are explored as potential solutions for managing temperature variations and peaks of high thermal loads in the Orion Multipurpose Crew Vehicle (Orion TCS) [5,6].

Spacecraft safety required phase change materials to meet a number of stringent constraints, such as low volume change during melting, low vapor pressure, low thermal expansion, low toxicity, and low reactivity with the container. As a result, hydration salts, pure salts and fatty acids are replaced by organic paraffins or eutectics of organic PCM materials. This approach allows for the incorporation of PCMs with a broad spectrum of phase change temperatures, coupled with relatively high latent heats [2,7]. In doing so, a diverse range of thermal requirements can be effectively addressed.

However, a significant drawback associated with organic phase change materials (PCMs) is their comparatively low thermal conductivity, rendering them less responsive to rapid thermal changes. The literature presents various solutions to address this issue, including the incorporation of metallic nanoparticles, utilization of micro-encapsulated PCM materials, or the implementation of aluminum fin lattices with different geometries [8,9]. In terrestrial applications, convective flows in the liquid phase address the problem of PCM low thermal conductivity. In microgravity PCM devices, thermocapillary (Marangoni) convection has been proposed as a means of heat transport [10], and parabolic flight experiments [11,12] have verified its potential improvement.

The initial motivation of the study was related to preparation of upcoming MarPCM/ISS experiment aimed to explore alternative

* Corresponding author.
E-mail address: berse@dtu.dk (B. Šeta).

https://doi.org/10.1016/j.icheatmasstransfer.2024.107741

Available online 11 July 2024

methods for optimizing heat management [1]. The prolonged period of microgravity aboard the ISS offers an opportunity to gain deeper insights into phase change dynamics and assess the improvement in heat transfer due to thermocapillary flows. In particular, it will examine the impact of Marangoni convection on the melting process in cuboidal or cylindrical geometries. Recent numerical studies were aimed at preparing a microgravity experiment to establish a solid scientific background [13–20]. These simulations played an important role in refining the experimental strategy, performing parameter sensitivity analysis, and ensuring that the MarPCM experiment will yield meaningful insights into the complex phenomenon of Marangoni convection.

Most numerical studies on thermocapillary effect in microgravity focused on high Prandtl number materials like n-octadecane. Simulations in 2D rectangular containers with differently heated walls examined melting phase bulk flow, influenced by container aspect ratio, wall temperature difference (Marangoni number), and heat loss through the interface [13,14,21]. In high aspect ratio containers, the flow begins as a stable single vortex, then changes to a multicellular structure and oscillatory hydrothermal waves at high Marangoni numbers. In low aspect ratio containers, a stable multicellular flow forms at low to moderate temperature differences (ΔT), becoming oscillatory as ΔT [13]. Recently, the different types of alkanes were also examined [15].

To understand the importance of the third dimension, a dedicated study was conducted comparing 2D and 3D numerical models [17,20]. This examination encompassed a number of the key parameters such as melting times, solid/liquid interface evolution, thermal fields, and spectrograms. The results showed that the transverse modes are often reflection symmetric about the midplane and have a relatively minor impact on the melting and PCM performance in most cases [20]. It was concluded that 2D results may be sufficient to provide a reasonably accurate approximation of the melting behavior at the mid-plane of the cuboidal domain at a lower computational cost.

Another geometry of interest is a cylindrical PCM configuration, where a solid cylinder is initially placed between two circular supports at different temperatures [17–19]. Three-dimensional results indicated that during the initial stage of melting, there is a noticeable increase in convection along the liquid edges due to the Marangoni effect. Meanwhile, the central part of the cylinder remains purely conductive. As more liquid forms, hydrothermal instabilities appear as standing and traveling waves with distinct frequencies and wave numbers. The complexity of the melting phase is such that, depending on ΔT, several traveling waves with different wave numbers, rotating in the same or opposite directions, can coexist. Marangoni convection enhances the heat transfer rate by about 1.7 times compared to purely conductive processes [19]. This improvement highlights the important role of Marangoni convection in enhancing heat transfer efficiency during the melting phase.

Low melting point metals, such as gallium, represent a new category of PCM characterized by excellent heat extraction capabilities due to their high thermal conductivity. The heat transfer performance of gallium during the melting phase was recently analyzed numerically under microgravity [22,23] and terrestrial conditions [24].

Recently, two studies simultaneously appeared that consider a thermoelectric energy harvester combining a thermoelectric generator with a PCM-filled unit having a free surface, aimed at potential spacecraft applications under extreme temperature variations [25,26]. One of them [25] deals with the melting phase of high Prandtl number PCMs (octadecane, hexadecane, and water), while the other [26] examines both the melting and solidification phases of low Prandtl number PCM (gallium) from both numerical and experimental perspectives.

However, the number of studies considering both the melting and solidification phases is very limited. In practice, thermal operations typically involve complete solid-liquid-solid conversion cycles. Addressing this gap is one of the objectives of this study.

Another aspect of novelty of the study lies in its investigation of the feasibility and effectiveness of various recovery strategies for phase change materials (PCMs) throughout complete solid-liquid-solid cycles, particularly focusing on gallium (*Ga*) and n-eicosane (C20).

We explore three different scenarios based on the temperature configuration between side walls before and after melting. We investigate how the efficiency of the PCM is influenced by the initially set heating direction. In addition, we reveal how the performance of PCM depends on the duration of the melting process.

2. PCM materials and geometry

In this study, two different materials are examined. The first one, Gallium (*Ga*), is chosen for its excellent thermal diffusivity and compatibility with stainless steel which is commonly used to fabricate PCM containers. With a very low Prandtl number ($Pr = 0.02$), it enables cost and time-efficient numerical simulations. Hence, it allows to consider multiple scenarios and guides simulations of PCMs with high Prandtl numbers.

The second material is a normal paraffin, n-eicosane (C20), which was proposed for upcoming experiments onboard the International Space Station (MarPCM project) [1]. Despite its relatively low thermal conductivity and high Prandtl number ($Pr = 51$), it has other properties that make it attractive for use in aerospace applications. The combination of its melting point close to room temperature, high specific heat capacity, latent heat storage capabilities and chemical stability makes n-eicosane a good candidate for PCM applications. The similar melting-point temperatures of Gallium and n-eicosane make them suitable candidates for drawing parallels in the results of numerical simulations. The insights obtained from simulations involving *Ga* can help understand how n-eicosane responds to changes in temperature, heat transfer rates, and other relevant parameters. Table 1 presents the main thermophysical properties of both materials.

Table 1
Thermophysical properties of the the Gallium [27–29] and Eicosane [7,15,30]. Here $\sigma_T = (d\sigma/dT)_{T_{ref}}$ and $\alpha_l = k_l/\rho_l c_{p,l}$ The subscripts m, l, and s stand for the melt, liquid and solid respectively.

Property	Symbol	Gallium (*Ga*)	Eicosane (C20H42)
Density [kg/m^3]	ρ_0	6093	775
Dynamic viscosity [kg/m· s]	μ_l	0.00181	0.00326
Thermal conductivity [W/m·K]	k_l/k_s	32.0/40.0	0.147/0.350
Specific heat [J/kg·K]	$c_{p,l}/c_{p,s}$	381.50/370.89	2315/1690
Thermal diffusivity [m^2/s]	α_l/α_s	$1.38{\cdot}10^{-5}/1.79{\cdot}10^{-5}$	$8.2{\cdot}10^{-8}$ /$2.67{\cdot}10^{-7}$
Latent heat [J/kg]	L_f	80,170	247,600
Liquidus/solidus temperature [K]	T_l/T_s	303.93/301.93	310.51/308.51
Melting temperature [K]	$T_m/$	302.93	309.51
Surface tension gradient [N/m·K]	σ_T	$-9.84 \cdot 10^{-5}$	$-9.75 \cdot 10^{-5}$
Prandtl number, $Pr = \nu/\alpha$	Pr	0.022	51.34
Marangoni number, $Ma = \lvert\sigma_T\rvert L\Delta T/\mu_l\alpha_l$	Ma	10,085	933,710

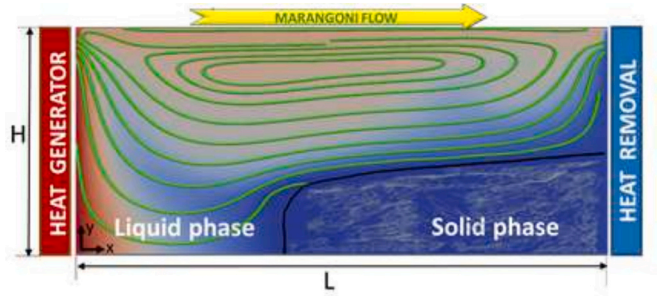

Fig. 1. Sketch of the problem ($L = 6.4$ cm, $H = 0.8$ cm).

3. Problem formulation

3.1. Governing equations

For the examination of the selected PCM materials, we consider a rectangular domain with the following dimensions $H = 0.8$ cm, $L = 6.4$ cm resulting in an aspect ratio, $AR = L/H = 8$ (see Fig. 1). The flow is considered laminar and the fluid is Newtonian, incompressible with constant thermophysical properties within the range of temperatures analyzed. The viscous dissipation and volume expansion caused by melting process are neglected. Assuming weightless conditions ($\vec{g} = 0$) the dynamics of the system is described the momentum and continuity equations:

$$\partial_t \vec{u} + (\vec{u}\cdot\nabla)\vec{u} = -\frac{1}{\rho_0}\nabla p + \nu\nabla^2\vec{u} + \frac{1}{\rho_0}\overleftarrow{DS}, \tag{1}$$

$$\nabla\cdot\vec{u} = 0 \tag{2}$$

here $\vec{u}$ represents the velocity vector $\vec{u} = (U_x, U_y)$, p is the buoyant pressure (the difference between total and hydrodynamic pressures), ρ_0 is the density at a reference temperature T_{ref} and $\nu = \mu_l/\rho_0$ is the kinematic viscosity.

The last term $\overleftarrow{DS}$ in momentum Eq. (1) represents the Carman-Kozeny model for a moving solid-liquid interface as a porous mushy layer where solid and liquid phases may coexist [31]. Thus, single momentum equation is solved for both liquid and solid phases (the solid one is fixed in place)

$$\overleftarrow{DS} = \frac{C(1-f_l)^2}{f_l^3 + b}\vec{u} \tag{3}$$

here f_l is a scalar field characterizing the local liquid fraction. It provides the coupling between the momentum and energy equations. This field depends on temperature and is bounded between zero (a pure solid) and unity (a pure liquid), i.e., $0 < f_l < 1$). In the regions where the solid and liquid are mixed together, the so-called mushy regions, the liquid fraction is not well-defined and should be approximated. The common approach to use a linear interpolation between the solidus temperature T_s and the liquidus temperature T_m.

$$f_l = \begin{cases} 0 & T \le T_s, \\ 1 & T \ge T_m, \\ \dfrac{T - T_s}{T_m - T_s} & T_s < T < T_m. \end{cases} \tag{4}$$

Here, we take $\delta T = 0.3$ K and the interface position is determined at intermediate value $f_l = 0.5$..

The value of the permeability (or Darcy) coefficient C in the $\overleftarrow{DS}$ term has a strong influence on behavior in the mushy region. Thus, the value of C is related to the morphology of the selected PCM and should be adjusted based on experimental results [32]. As in previous works [10,18,19], the value of C is set to 1.6×10^6 kg m^3 s. The small constant $b = 10^{-3}$ in the DS term is added to this term to prevent division by zero when $f_l = 0$; its choice is arbitrary.

The energy equation takes into account the heat transfer and the phase change (latent heat L_f):

$$\frac{\partial(c_p T)}{\partial t} + \vec{u}\cdot\nabla(c_p T) = \frac{1}{\rho_0}\nabla^2(kT) - L_f\frac{\partial f_l}{\partial t} \tag{5}$$

where c_p and k are the weighted specific heat and thermal conductivity defined as

$$(c_p, k) = (c_{ps}, k_s)(1 - f_l) + (c_{pl}, k_l)f_l. \tag{6}$$

3.2. Boundary conditions

The problem formulation should be completed with boundary and initially conditions. No-slip boundary conditions are applied to all boundaries except the upper one, where Marangoni convection occurs. The top and bottom walls are considered under adiabatic conditions, while the endwalls are maintained at constant but distinct temperatures. The given sets of temperatures are discussed in frame of different strategies for melting and solidification phases.

Initially, the materials are in a solid state, having a uniform temperature below the melting point, $T_s = T_m - 1.5$ K. The melting process begins when $\Delta T = 40$ K is applied at the left wall while the temperature on the right wall depends on the case (see Fig. 1). After the system has reached steady state, in order to initiate the solidification process, the boundary temperatures on the left or right walls are changed [33]. Three different sets of boundary conditions for melting and solidification phases are considered, which are outlined in Fig. 2. The initial conditions for the melting phase at the initial moment are (here $\delta T = 0.3$ K):

$$\#1 \quad \begin{aligned} T(x=0) &= T_m + \Delta T, \\ T(x=L) &= T_m + \delta T \end{aligned} \tag{7}$$

$$\#2 \quad \begin{aligned} T(x=0) &= T_m + \Delta T, \\ T(x=L) &= T_m + \delta T \end{aligned} \tag{8}$$

$$\#3 \quad \begin{aligned} T(x=0) &= T_m + \Delta T, \\ T(x=L) &= T_m - \Delta T \end{aligned} \tag{9}$$

At the onset of solidification process the boundary conditions for different cases are the following

$$\#1 \quad \begin{aligned} T(x=0) &= T_m + \Delta T, \\ T(x=L) &= T_m - \Delta T \end{aligned} \tag{10}$$

$$\#2 \quad \begin{aligned} T(x=0) &= T_m - \Delta T, \\ T(x=L) &= T_m + \delta T \end{aligned} \tag{11}$$

$$\#3 \quad \begin{aligned} T(x=0) &= T_m - \Delta T, \\ T(x=L) &= T_m + \Delta T \end{aligned} \tag{12}$$

The surface tension σ of a liquid is temperature dependent and defined as:

$$\sigma = \sigma_{ref} - \sigma_T(T - T_{ref}), \tag{13}$$

where $\sigma_T = (d\sigma/dT)_{T_{ref}}$ is the surface tension gradient coefficient. The temperature gradient creates a surface tension gradient at a growing liquid/air interface that induces a thermocapillary flow in the melted liquid and surrounding air (although the latter is not considered). This convection provides a mechanism for heat transport in microgravity, which modifies the melting dynamics and heat transfer via the free surface. Thus the boundary condition on the PCM/gas interface $y = H$ is the balance of viscous and thermocapillary forces

$$\mu\frac{\partial\vec{u}}{\partial n} = \sigma_T\frac{\partial T}{\partial\tau} \tag{14}$$

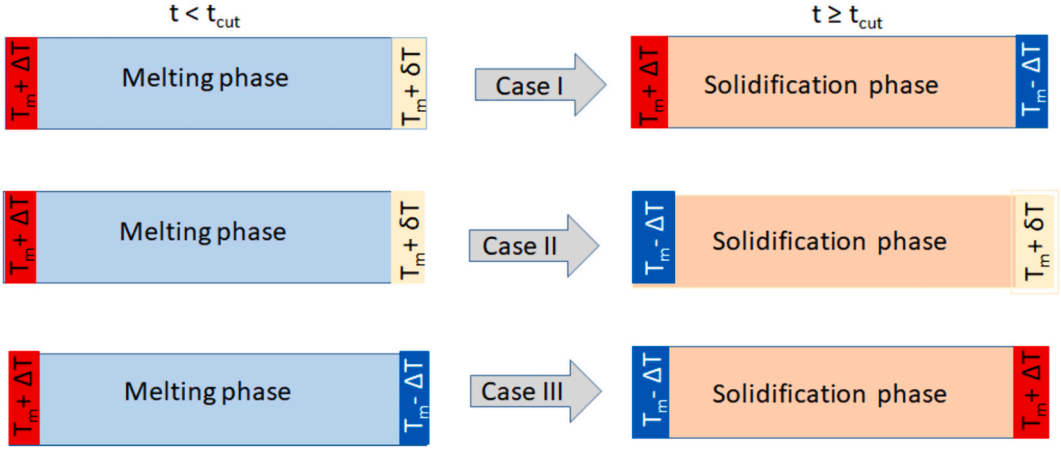

Fig. 2. Boundary conditions for the melting and solidification phases for the various cases studied ($\Delta T = 40$ K and $\delta T = 0.3$ K). At the *melting phase*, the temperature on the left side is the same in all cases, $T_m + \Delta T$. On the right side, the temperature in the first and second cases is slightly higher than the melting temperature $T_m + \delta T$ while in the third case, the temperature is strongly decreased relative to T_m, i.e., $T_m - \Delta T$. At the *solidification phase*, the temperature on the left does not change in case I, but on the right, it decreases greatly, $T_m - \Delta T$. In cases II and III, the temperature on the left side decreases by the same amount ΔT, but on the right side, the temperatures are different, $T_m + \delta T$ and $T_m + \Delta T$, respectively.

where $\partial/\partial n$ and $\partial/\partial \tau$ are the derivatives in the normal and tangential directions. To quantify the strength of Marangoni convection, the non-dimensional Marangoni number is introduced

$$Ma = |\sigma_T| L \Delta T / \mu_l \alpha_l. \quad (15)$$

Since in this study we use only one value of $\Delta T = 40$ K, the corresponding Marangoni numbers for gallium and eicosane are given in Table 1.

3.3. Numerical approach

The OpenFOAM package is used to solve the problem defined above. The PIMPLE algorithm was considered to solve the momentum and continuity equations as it guarantees a correct pressure-velocity coupling. The temperature was calculated in each PIMPLE iteration. The final system of linear equations was solved using the preconditioned bi-conjugate gradient, PBiCG, method with a common tolerance of 10^{-8} for pressure, velocity and temperature fields.

The numerical solver uses second-order schemes for space and time discretization. The rectangular domain was divided in (200×40) cells with $\Delta x = 3.2{\cdot}10^{-4}$ m and $\Delta y = 2{\cdot}10^{-4}$ m. The time step used for the simulation was set at 1 ms to ensure the numerical stability. The numerical code and grid convergence have been validated in our previous publications [17–20]. Details about the validation of the code, based on extensive comparisons with positive and negative surface tension systems as well as the phase change in experiments using gallium [34] in a rectangular cavity heated from one side, can be found in [17]. The rationale for the grid independence check and the time step selection were presented in detail in our recent publication [19].

4. Results

4.1. Case 1, gallium

Here we consider a low Prandtl number material, gallium, which will also serve as a reference for high Prandtl number eicosane. Each case considered includes two phases: melting and solidification. In case I (see Fig. 2), after the completion of melting at $t = 636$ s, the temperature at the initially cold wall ($x = L$) decreased sharply by $\Delta T = 40$ K, triggering the solidification of the PCM. Recall that the temperature of the hot wall ($x = 0$) remained constant throughout this process. To determine the time evolution of the heat transfer rate either through hot (left) or the cold (right) wall, the local heat flux, $q = -k\partial T/\partial x$, is integrated

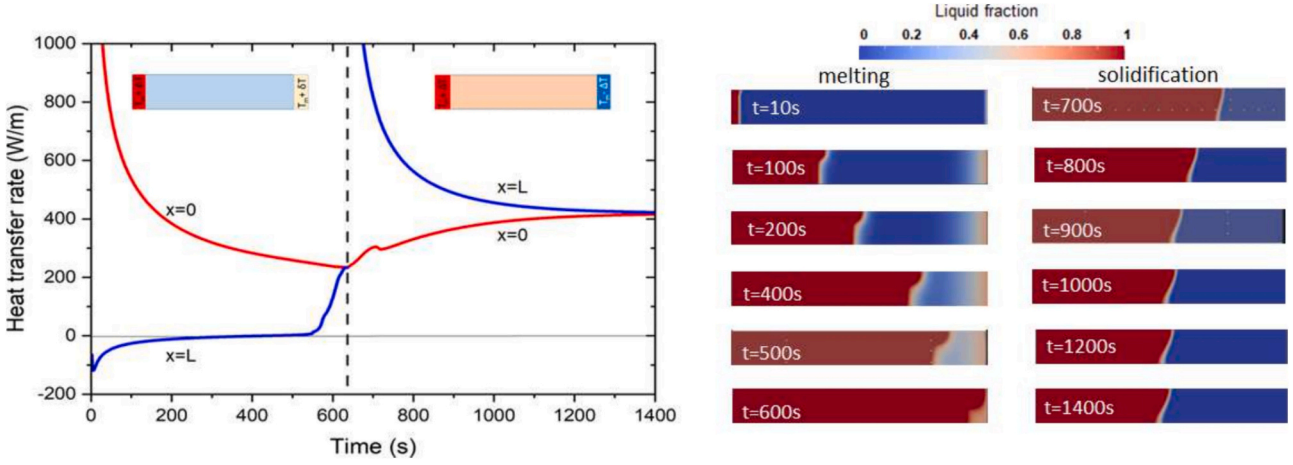

Fig. 3. *Case I for Ga.* Time evolution of the heat transfer rates at the hot (red curve) and cold (blue curve) walls for the complete cycle. The vertical black solid line marks the transition between the melting and solidification phases. The two series of snapshots show the solid-liquid interface evolution during melting and solidification at selected times. (For interpretation of the references to colour in this figure legend, the reader is referred to the web version of this article.)

over the height H :

$$Q = -\int_0^H k(\partial T/\partial x)_{x=0,L}\, dy$$

where k is the average thermal conductivity of the material, see Eq. (6). A positive value for heat transfer indicates heat gain by the system. In the considered geometry, the positive value of Q corresponds a heat flux entering to the system through the hot disk.

Fig. 3 presents the time evolution of Q at both lateral walls. The left part of the figure shows the development of melting-solidification processes at selected points in time. As gallium melts, the heat extraction performance gradually reduces at the hot wall ($x = 0$), tending to an asymptotic value of 240 W/m when the material is fully melted. Note that this value is only 50% higher than expected from a pure conductive mechanism ($Q_{cond} = k_l \Delta T H/L = 160$ W/m). Due to the relatively high thermal conductivity of gallium, conduction is more efficient than Marangoni convection. Nevertheless, Marangoni convection still makes a significant contribution. Its presence is confirmed by the observed interface profile at later times, where a non-parallel alignment to the side walls indicates the existence of convection.

At the cold plate ($x = L$), the heat transfer rate exhibits weak negative values during the melting phase, which is a consequence of the slightly elevated temperature imposed at the cold wall, $T_m + \delta T$. At approximately 550 s, when the liquid/solid front approaches the cold wall, the heat transfer rate suddenly changes to a positive value. This change is the result of the system temperature exceeding the cold wall temperature.

At the time all the gallium has melted ($t_{cut} = 636$ s), the boundary condition on the cold wall switches to $(T_m - \Delta T)$ (see Fig. 2), initiating the solidification process. As soon as fluid near the cold plate solidified, the heat fransfer rate through it sharply increased up to 1000 W/m. Afterward, this value exponentially decreases tending to converge to the value at the hot plate, which is 420 W/m. In the context of the complete solidification phase, the heat extracted from the hot wall gradually increases. Starting from an initial value of 240 W/m, the heat transfer rate approaches the asymptotic value of 420 W/m in a steady state.

The solid-liquid interface moves towards the hot plate, stabilizing its position at approximately half the volume ($f_l \sim 0.52$). This position of the interface is consistent with the symmetrical distribution of temperatures in the domain, i.e., $(T_m + \Delta T)$ at the hot wall and $(T_m - \Delta T)$ at the cold wall, $\Delta T = 40$ K. Under these conditions, the location of the solid-liquid interface remains practically unchanged, as the heat flux extracted from the hot plate is transferred to the cold plate. This interface position is illustrated by snapshots at at the right part of Fig. 3. Note that the difference between the heat transfer rate at both extreme walls during the complete cycle was associated to the latent heat used to melt the PCM.

The stability of the liquid-gas interface at the position $x_0 = 0.52L$ allows the heat transfer through the solid and liquid parts to be evaluated separately. Since gallium has high thermal conductivity, it is assumed that the temperature profile in the horizontal direction varies linearly. Then, in the steady state the heat transfer rate through the volume occupied by the liquid phase is $Q_l = k_l \Delta T_l H/0.52L = 320 W/m$, and through the solid part $Q_s = k_s \Delta T_s H/0.48L = 406 W/m$, correspondingly. The comparison of these simple estimations suggests that conduction is the predominant mechanism governing heat transfer in gallium.

To highlight the role of Marangoni convection in heat transfer, an additional analysis is suggested based on the time evolution of the liquid fraction throughout the process. Assuming a simple 1D pure conductive model (which is reasonable in this case), the time evolution of the solid-liquid interface position, x_0, was obtained (See Supplementary material)

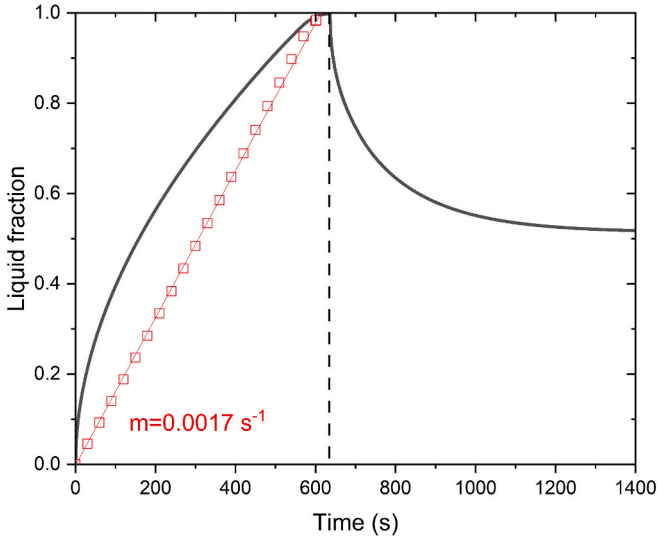

Fig. 4. *Case I for Ga.* Time evolution of the liquid fraction. The black curve represents the results of the direct simulations for the entire melting-solidification cycle. The red open symbols and their linear fit depict the squared liquid fraction calculated at given points from data on the black curve only for the melting phase. The slope of the red line written in the graph is compared with that one in Eq. (16). Both demonstrates that the liquid fraction spreads as $\sqrt{(t)}$. (For interpretation of the references to colour in this figure legend, the reader is referred to the web version of this article.)

$$\frac{(x_0)^2}{L^2} = \frac{2k_L \Delta T}{\rho\left[L_f + 0.5 c_{p,l}\Delta T + (c_{p,l} - c_{p,s})T_m\right]L^2} t = 1.13{\cdot}10^{-3} t \tag{16}$$

where (x_0/L) is the normalized distance from the hot wall, which is is equivalent to the liquid fraction. This dependence aligns with the solution of the Stefan problem, indicating that the position of the boundary shifts in accordance with the square root of time $\sqrt{(t)}$.

Fig. 4 illustrates the time evolution of the liquid fraction throughout the complete cycle. The red symbols on the graph represent the squared liquid fraction calculated at several points based on numerical data. This representation demonstrates that the liquid fraction spreads as $\sqrt{(t)}$. The linear fit of these points allows for comparison between the slope obtained from direct numerical simulations and the one calculated using Eq. (16). The slope obtained from direct simulations is $1.7{\cdot}10^{-3} s^{-1}$, which is higher than the $1.13{\cdot}10^{-3} s^{-1}$ value determined from the 1-D simplified model. In addition, the melting time predicted by the above model is $t = 854$ s (when $x_0 = L$), which is longer than that obtained from the simulation ($t = 636$ s). This observation indicates that the solid-liquid interface evolvesat a faster rate than predicted by the pure conduction model, primarily due to the Marangoni contribution. Hence, the pure conductivity model is ineffective in this case.

A similar one-dimensional approach was utilized to analyze the influence of Marangoni effect during the solidification phase. The model neglecting the Marangoni contribution provides that the solid-liquid interface stabilizes at $x_0/L = 0.44$. However, according to simulations of the full problem, the liquid/solid front stabilizes at a distance of $x_0 = 0.52L$ from the hot wall. The discrepancy in the interface position (0.44 L versus 0.52 L) means that the thermocapillary effect cannot be neglected throughout the cycle.

For a continuous heat extraction, the above cycle must be repeated taking into account the conditions in the steady state. As the PCM gradually melts, the solid-liquid interface will shift towards the cold plate. The heat transfer rate at $x = 0$ gradually falls from 420 W/m to

240 W/m, (see Fig. 3) due to the low temperature gradients near the hot plate, without considering the positive contribution of the transient phase occurring in the first instants of the first cycle (from 1000 W/m to 420 W/m). Therefore, it can be concluded that the proposed strategy does not optimize the long-term efficiency of the heat exchanger.

4.2. Case II, gallium

During the melting phase the temperatures of both walls is identical to the case I presented above, i.e., $T(x=0) = T_m + \Delta T$ and $T(x=L) = T_m + \delta T$, see Fig. 2. In the solidification phase the temperature of the hot wall is dropped below the melting point $(T_m - \Delta T)$, maintaining the temperature of the cold wall at $(T_m + \delta T)$, as above $\Delta T = 40$ K and $\delta T = 0.3$ K.

Fig. 5 shows the evolution of the heat transfer rate on both hot and cold walls, as well as snapshots of the melting-solidification processes at selected points in time. In the melting phase, the heat transfer rate at both walls is identical to that in the first scenario and shown in Fig. 3. Once the hot plate starts to cool down ($t_{cut} = 636$ s), a strong outflow is developed at $x = 0$, provoking the solidification of the PCM. During this process, the solid-liquid interface remains flat and perpendicular to the heat flux direction, as evident from a series of snapshots in Fig. 5. This flatness is a distinctive feature indicating the absence of Marangoni flow. Marangoni flow is inhibited because the liquid phase remains nearly isothermal at $T = T_m$. The absence of temperature gradients in this region nullifies heat transfer at $x = L$ until the solid/liquid front reaches the cold wall ($t = 1300$ s). Then the heat flux at $x = L$ decreases sharply, aligning with that of the $x = 0$ wall (approximately 200 W/m), corresponding to a pure conduction between the two walls.

To complement these results, Fig. 6 presents the time evolution of the liquid fraction for the complete cycle. Here we focus attention on the solidification phase. The red symbols on the graph represent the squared solid fraction calculated at specific points, along with their corresponding linear fit. This linear fit provides a comparison between the slope determined from direct numerical simulations and the that one using 1D model, see supplementary material. The simplified model provides that the solid fraction during the solidification process varied as follows:

$$\frac{(L-x_0)^2}{L^2} = \frac{2k_s\Delta T}{\rho\left[L_f + (c_{p,s}\Delta T)/2 + (c_{p,l} - c_{p,s})T_m\right]L^2}\, t = 1.54{\cdot}10^{-3} t \tag{17}$$

The slope obtained from Eq. (17) perfectly matches with that from the direct numerical simulations as follows from Fig. 6 where the value of slope is written on the graph; compare $1.54{\cdot}10^{-3}$ (1D) and $1.5{\cdot}10^{-3}$ (CFD).

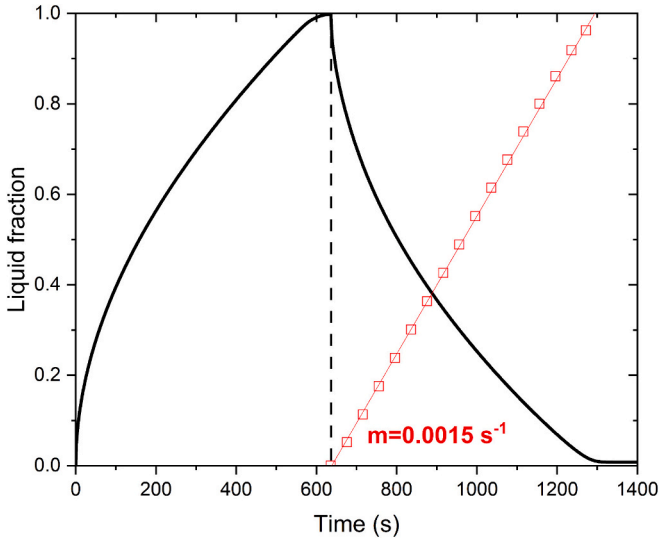

Fig. 6. *Case II for Ga.* Time evolution of the liquid fraction for the complete cycle (the black solid curve). The red open symbols depict the squared solid fraction, i.e., $(L - x_0)^2$, calculated at given points for comparison with Eq. (17). The red line represents a linear fit to the symbols. (For interpretation of the references to colour in this figure legend, the reader is referred to the web version of this article.)

Reheating the left side once more, up to $(T_m + \Delta T)$, restores the temperature boundary conditions to precisely the initial scenario, inducing a similar behavior of the heat rate transfer as discussed above. This is characterized by rapid melting near the hot wall, promoting an efficient heat extraction. Nevertheless, this performance quickly decreases reaching the asymptotic value of approximately 240 W/m, which is quit close to fully conductive behavior within the liquid phase. For continuous heat extraction, this scenario is feasible, albeit the Marangoni contribution is limited. However, from a technological standpoint, this seems unrealistic, since it requires more than two heat sources, which complicates the real design. Therefore, this approach does not optimize the heat extraction process.

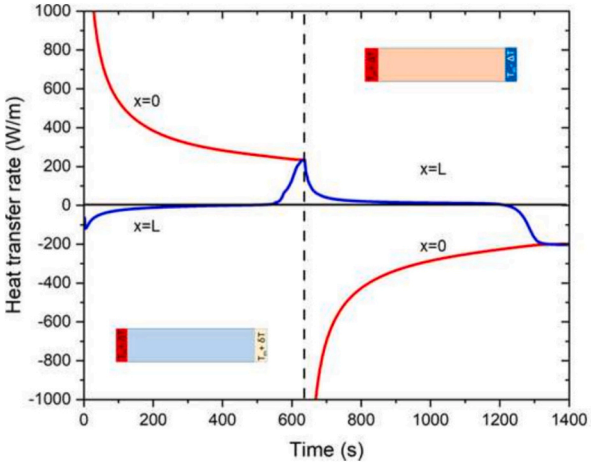

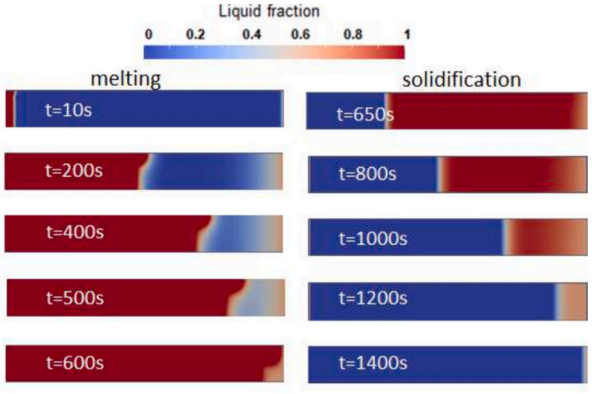

Fig. 5. *Case II for Ga.* Time evolution of the heat transfer rates at the hot (red curve) and cold (blue curve) walls for the complete cycle. The vertical black solid line marks the transition between the melting and solidification phases. The two series of snapshots show the solid-liquid interface evolution during melting and solidification at selected times. The snapshots are not equidistant and are shown at the most representative time moments. (For interpretation of the references to colour in this figure legend, the reader is referred to the web version of this article.)

4.3. Case III, gallium

4.3.1. A single temperature inversion of PCM

In the third case, the initial boundary temperature condition at the left wall ($x = 0$) remains consistent with those of the two previous scenarios, i.e., ($T_m + \Delta T$), while a change is introduced at the right wall where the initial boundary temperature is set at ($T_m - \Delta T$). Consequently, the temperature gradient is doubled ($2\Delta T/L$). At $t_{cut} = 636s$, corresponding to the onset of the solidification process in Case I and Case II, a temperature inversion is imposed between the two walls. It is worth noting that in case III at this point in time only about half of the PCM has been melted. Nevertheless, the temperature of the hot wall decreases to ($T_m - \Delta T$), while the cold wall temperature increases to ($T_m + \Delta T$) (see Fig. 2). Technically, this procedure is mimicking the rotation of the PCM body between two fixed temperature sources after $t_{cut} = 636s$..

Computed heat transfer rate and the liquid-solid interface position, x_0, are presented in Fig. 7. Until t_{cut}, the heat transfer rate at $x = 0$ continuously decreases and stabilizes at a level of about 400 W/m. This value is much higher than in previous cases due to duplication of the temperature gradient. The behavior of the flux at $x = L$ differs significantly from previous cases, since it stably maintains a positive value. This is a consequence of the freezing condition imposed at the right boundary. At $t_{cut} = 636$ s, the inversion of temperatures at both walls causes a reversal in the direction of heat flux. As depicted in the left panel of Fig. 7, a rapid and sharp decline in the heat transfer rate occurs at both walls over a short time interval, lasting approximately 200 s. Following this, the rates the rates quickly converge towards an asymptotic value of about 400 W/m. Consequently, the difference between the heat transfer rates at both walls becomes negligible.

After temperature switch, solidification starts at $x = 0$, while melting commences at $x = L$, as illustrated by the snapshots in Fig. 7. They illustrate that the distribution of the liquid fraction undergoes a notable change within the initial $\sim$ 200 s after the temperature switch. During this period, the molten and solid regions alternate along the length of the cavity, converging towards the stable position of a single interface, approximately at $x_0 \sim 0.5L$..

A detailed view of the flow dynamics 15 s after the temperature switch is presented in Fig. 8. The Marangoni number is used to quantify the strength of the flow, which is

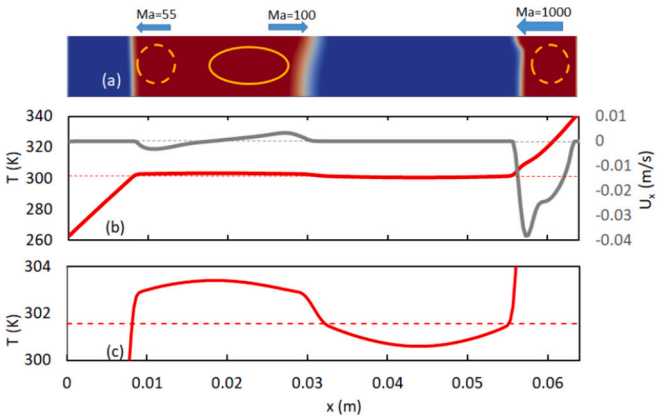

Fig. 8. *Case III for Ga.* Flow dynamics shortly after switching temperature at the bounding walls, $t = 650$ s. (a) A snapshot illustrating alternating liquid and solid zones and sketch the flow pattern. The arrows indicate the direction of the flow. (b) Velocity (the gray curve) and temperature (the red curve) profiles at the gallium interface, elucidating strong flow near the right wall associated with the high Marangoni number. (c) Magnified view of the temperature profile at the central part of the cell, which is nearly invisible in panel (b). (For interpretation of the references to colour in this figure legend, the reader is referred to the web version of this article.)

$$Ma = \frac{|\sigma_T| h^* \Delta T^*}{\mu \alpha}. \tag{18}$$

where h^* is the length of liquid zone under local temperatures gradient ΔT^*..

The temperature profile exhibits nearly linear behavior near the side walls in regions with an aspect ratio close to unity. Correspondingly, the peak velocity occurs near the right wall, where the Marangoni number reaches its highest value, $Ma \sim 1000$, see the gray curve in panel (b). This strong flow leads to the deformation of the interface shape. Near the left wall, the phase change material is already solidified. The temperature change in most of the cavity is negligible, amounting to only 5% of the applied temperature difference. To shed light on this behavior, panel (c) provides a magnified view of the temperature in this region. Due to to small temperature gradients at the edges of the left liquid zone, the flow

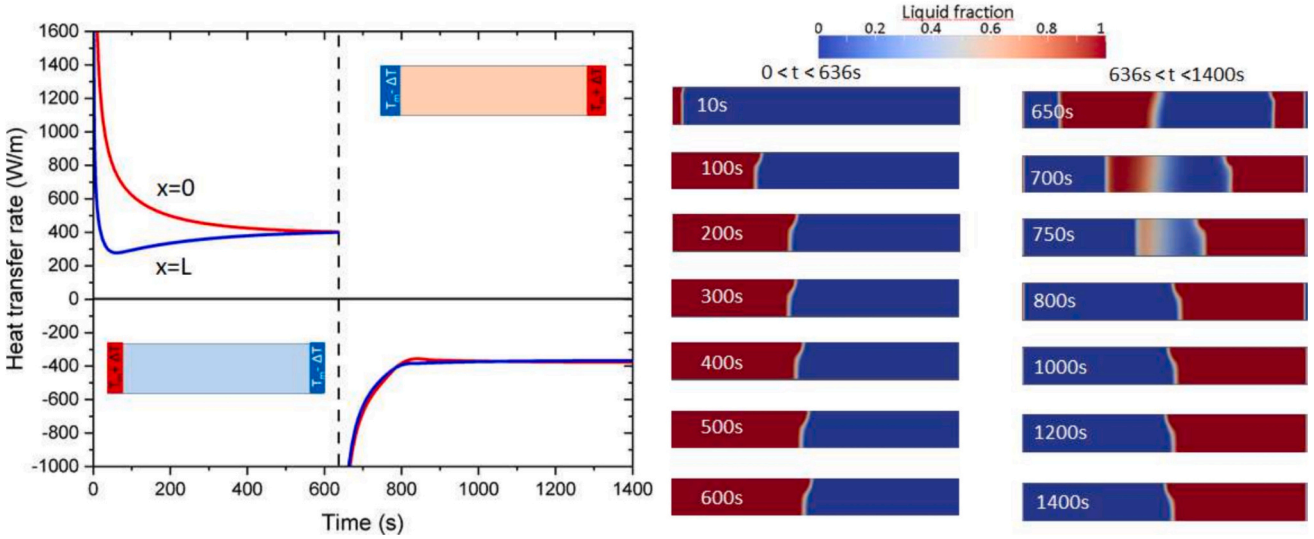

Fig. 7. *Case III for Ga.* Time evolution of the net heat transfer rates at the hot (red curve) and cold (blue curve) walls for the complete cycle. The vertical black solid line at $t = 636$ s marks the switching of boundary conditions. The two series of snapshots show the solid-liquid interface evolution at selected times before and after switching of boundary conditions. The snapshots are not equidistant and are shown at the most representative time moments.] (For interpretation of the references to colour in this figure legend, the reader is referred to the web version of this article.)

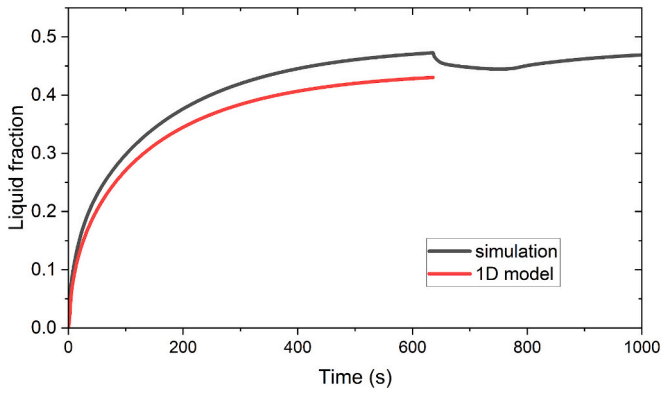

Fig. 9. *Case III for Ga.* The temporal evolution of the liquid fraction throughout the entire cycle. The black and red curves represent the predicted results of the direct simulations and the 1D model, respectively. (For interpretation of the references to colour in this figure legend, the reader is referred to the web version of this article.)

in this region is weak. Furthermore, the two vortices exhibit opposing circulations and strengths due to temperature gradients of different signs and values at the local liquid/solid interfaces.

The time evolution of the solid-liquid interface position, denoted as x_0, during the melting process could be modeled similarly to the approach described earlier, see Eq. (16). The derivation of equation for the interface displacement, can be found in Supplementary materials. Here we present the results only in graphical form. The evolution of the interface position is illustrated in Fig. 9 by a continuous red curve. The values obtained from the 1D model are slightly lower than the computed ones, indicating an underestimation of the incoming flux. To align these two sets of values, a coefficient of 1.15 must be applied to the red curve.

This scenario appears to be quite advantageous as it enhances the overall heat extraction efficiency. The success of this scenario involving temperature switching relies on the existence of symmetric thermal boundary conditions. However, this requires an inversion of the heat transfer direction, and realistic implementation can be challenging. To avoid this inconvenience, the authors propose, upon reaching $t_{cut} = 636$ s, to rotate the PCM body by 180°, while maintaining the temperature on the external walls fixed ($T_m + \Delta T$ at $x = 0$, and $T_m - \Delta T$ at $x = L$). This rotation is formally equivalent to the switching of temperature conditions in Case III.

4.3.2. Multi-cyclic PCM temperature inversion

To simplify understanding, in this and following sections, the inversion of temperature on the walls will be referred to as the rotation of the PCM body inside the package. Although in the numerical simulations, the temperature is actually inverting. Thus, the coordinate system remains fixed with respect to the heat sources, while the PCM material has the capability to rotate within the cavity. As follows from Fig. 7, the heat extraction efficiency drops after 200 s, therefore the rotation of the PCM body should be set to this time step in order to benefit the high heat extraction rate in the early moments. Moreover, the suggested rotation concept has the potential to simplify the technological design of the system and facilitate its manipulation.

Fig. 10 presents the heat transfer rate under the above conditions. The rotation of the PCM every 200 s ensures that the solid phase comes into contact with the hot plate, while the liquid phase contacts the cold plate. This leads to an increase in the heat flux by enhancing the latent heat contribution as a result of the multiple phase change steps at both the hot and cold walls. Note that at the melting stage, the heat transfer rate at the cold wall is significantly lower than at the hot wall (x = 0), although converging the same value in the steady state. The observed behavior disappears when the melting process is repeated. The heat fluxes at all stages become highly similar. A comparison of the blue and

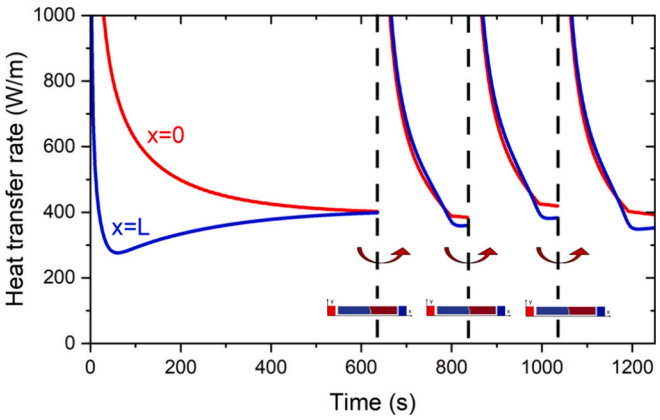

Fig. 10. *Case III for Ga.* Temporal evolution of the net heat transfer rate at $x = 0$ (red) and $x = L$ (blue) at different steps. The first step lasts 636 s and then the PCM material undergoes rotation every 200 s within the cavity. The dark red arrows depict the moments of rotation. Throughout the process, the temperatures at the cavity walls remain fixed. Small sketches of the cavity with PCM temperature are included to enhance understanding. (For interpretation of the references to colour in this figure legend, the reader is referred to the web version of this article.)

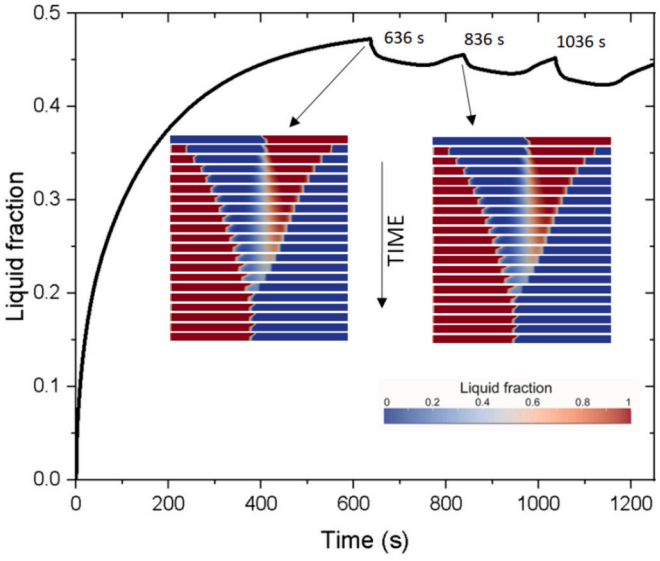

Fig. 11. *Case III for Ga.* Evolution of liquid fraction with PCM rotation. The solid black line represents the progress of the liquid fraction over time as the PCM material rotates at $t = 636$ s, 836 s and 1036.Two inserts provide series of snapshots illustrating the distribution of liquid and solid phases in two cases: after rotation at t = 636 s and 836 s. The snapshots are given at equidistant time intervals. After the first rotation, the first snapshot is shown at $t = 636$ s, followed by subsequent snapshots at intervals of $\Delta t = 10$ s. Similarly, after the second rotation the first snapshot corresponds to $t = 836$ s and then the rest is given with the same step $\Delta t = 10$ s.

red curves in Fig. 10 reveals that approximately 130 s after PCM rotation, once the steady state is approaching, the heat transfer rates at both walls converge to different values, with the heat flux at $x = 0$ being slightly higher.

Fig. 11 depicts the evolution of the liquid fraction over time while the PCM undergoes rotation at specific time moments. Upon reaching $t = 656$ s, the liquid fraction experienced a slight decline, reaching a minimum value of 0.44 around 750 s, before gradually increasing to 0.46 after 200 s (at $t = 836$ s). This trend persists after each subsequent PCM rotation. Analysis of the snapshots reveals the presence of two distinct fronts, solid and liquid at each half-cell, both advancing towards the

center of the PCM box at approximately equal velocities. Features of the flow pattern shortly after the temperature switch were discussed in Fig. 8. This observation suggests that the heat transfer rates at both walls $x = 0$ and $x = L$ are similar, resulting in minimal variation in the liquid fraction.

5. n-Eicosane

As mentioned earlier, the optimal performance of PCM involves symmetric thermal boundary conditions and multi-cyclic temperature inversion. For explanation purposes, we mimic this regular temperature switching by rotating the PCM within the package while maintaining fixed wall temperatures. Recall, that in the numerical simulations, the temperature is actually inverting. This strategy, previously successful with gallium, is now being applied to n-eicosane (C20H42, also known as C20 in its solid state) using the same geometry. Note that the thermal conductivity of n-eicosane (C20) is significantly lower than that of gallium having 100 and 200 times lower values for the solid and molten phases, respectively. Despite this contrast, the Marangoni numbers for both materials are somewhat similar. Consequently, it is anticipated that Marangoni convection will dominate over conductive heat transfer.

Fig. 12 illustrates the heat transfer rate at both walls, x = 0 (the hot wall with temperature $T_m + \Delta T$) and x = L (the cold wall with temperature $T_m - \Delta T$), over several rotations of the PCM box, here $\Delta T = 40$ K as above. The first rotation of the box takes place at $t = 3350$ s, when the steady state is reached, followed by successive repetitions occurring every 1000 s. Fig. 13 presents the evolution of liquid fraction at selected times along with corresponding snapshots.

The heat transfer behavior of C20 at $x = 0$ differs significantly from that of Gallium. Initially, the heat flux at the hot wall drops down to 60 W/m in 200 s, which is much faster than in the case of Gallium. It then increases, reaching a maximum value 68 W/m at approximately 2000 s, see red curve in Fig. 12. This increase is associated with additional heat transfer by Marangoni convection and ceases when the upper part of the solid-liquid front approaches the cold wall. As the system reaches a stationary state, around 3400 s, the heat transfer rate stabilizes at 50 W/m. The overall behavior is largely influenced by Marangoni convection, which prevails over weak conduction. When subjected to a

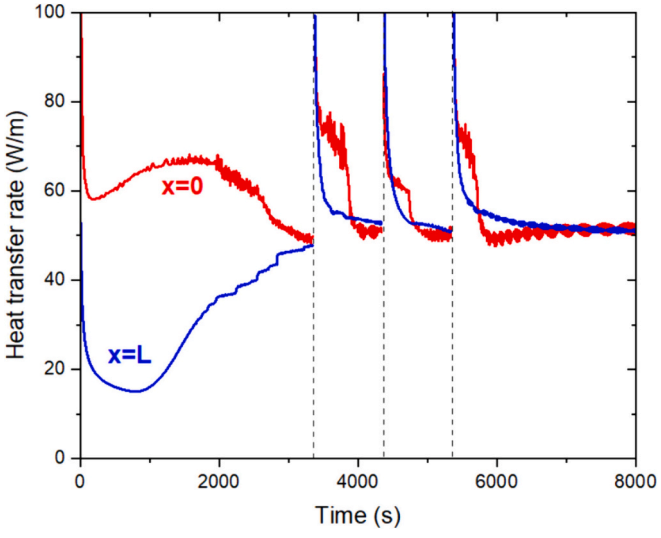

Fig. 12. *Case III for n-eicosane.* (a) Temporal evolution of the heat transfer rate at $x = 0$ (red) and $x = L$ (blue) at different steps. The first step lasts 3350 s and then the PCM material undergoes rotation every 1000 s, i.e. at $t = 3350$ s, $t = 4350$ s and $t = 5350$ s. The duration of the last step is elongated to illustrate oscillatory behavior when the liquid friction becomes important. (For interpretation of the references to colour in this figure legend, the reader is referred to the web version of this article.)

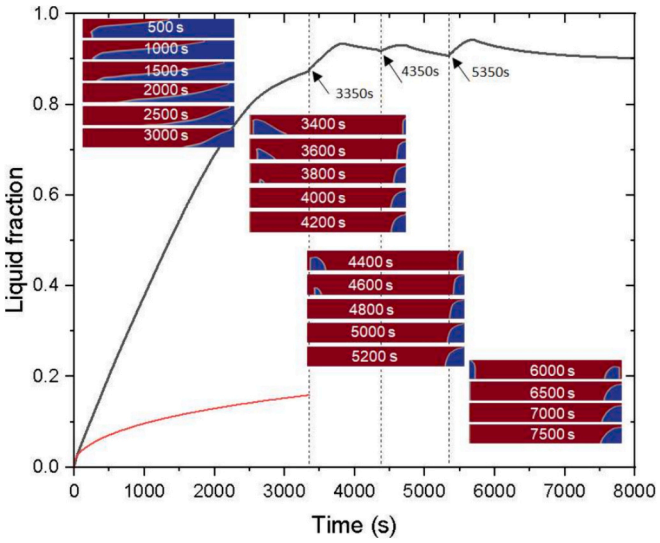

Fig. 13. *Case III for n-eicosane.* Evolution of liquid fraction. The solid black line represents the progress of the liquid fraction over time as the PCM material rotates at $t = 3350$ s, $t = 4350$ s and $t = 5350$ s. Inserts illustrate the distribution of liquid and solid phases at given time moments. The red curve in panel (b) depicts the expected heat transfer rate under conditions of pure conduction. (For interpretation of the references to colour in this figure legend, the reader is referred to the web version of this article.)

thermocapillary flow, the solid/liquid front undergoes significant elongation, particularly evident in the upper part of the cell, as illustrated by the snapshots of the liquid fraction in Fig. 13. This observation is supported by the calculation of the heat transfer rate through pure conduction ($k_l L_f \Delta T/L = 1.48$ W/m), which demonstrates its minimal contribution in comparison to the net value 50 W/m. The heat transfer at $x = L$ resembles that observed in Gallium. This solid region remains unaffected by Marangoni convection. Heat transfer decreases to 15 W/m at $t = 1000$s and then grows up until it equals the data at $x = 0$.

When examining the evolution of the liquid fraction of C20 (Fig. 13, significant differences are observed compared to *Ga*. While the liquid fraction in the the case of *Ga* asymptotically approaches to about 0.5 (see Fig. 9), it tended to reach 0.9 for C20. This clearly indicates the substantial involvement of Marangoni convection in the entire heat transfer process in the liquid phase. Furthermore, this discrepancy is also highlighted by the time evolution of the liquid fraction expected from 1D model shown by the red curve in Fig. 13.

After t = 3350 s, the PCM is rotated by 180° three times consecutively, each 1000 s. The behavior of the heat flux in both cases, *Ga* and C20, is similar, both reaching high mean values for their heat transfer rates. However, during the transient regime, this case shows larger differences between the heat fluxes at opposite walls compared to gallium, indicating a more asymmetric melting/solidification regime at both boundaries. Note that the latent heat involved in the phase change process affects only a small part of the domain near the cold and hot walls, contrasting with gallium, where almost all the bulk participated in the phase change (see Fig. 11). The presence of a large liquid zone throughout the melting process for C20 actively contributes to heat transfer by transporting the hot material via Marangoni convection from the hot to the cold wall.

6. Conclusions

We have examined the heat transfer rates in Phase Change Materials (PCMs) throughout complete solid-liquid-solid conversion cycles. Two materials are examined: Gallium (*Ga*) and n-eicosane (C20), which was proposed for upcoming experiments onboard the ISS (MarPCM project) [1]. The characteristic thermal time for n-eicosane, $\tau_{th} = L^2/\alpha = 5{\cdot}10^4$,

is substantial, indicating a relatively long time scale for thermal diffusion. Consequently, simulations involving n-eicosane require extensive computational time to accurately resolve the heat transfer processes within the material. In contrast, Gallium exhibits a much shorter characteristic time, $\tau_{th} = 3{\cdot}10^2$ s, facilitating efficient numerical simulations and enabling consideration of multiple scenarios. The similar melting-point temperatures of *Ga* and n-eicosane make them suitable for drawing parallels in numerical simulation results, offering insights into n-eicosane's response to temperature changes.

The novelty of our study lies in its multifaceted approach, encompassing the consideration of both melting and solidification phases, the analysis of different temperature scenarios, an assessment of practical implementation aspects, and the investigation of Marangoni convection.

Three different scenarios characterized by various temperature configurations between the endwalls before and after melting are explored employing *Ga*. The primary objective is to ascertain the most effective scheme for optimizing PCM performance in repeated solid-liquid-solid conversion cycles. Among the examined cases, the Case III with symmetric boundary conditions and multi-cyclic temperature inversion turned out to be the most advantageous, significantly enhancing overall heat extraction efficiency. In this case, initial temperatures of the hot and cold walls were set to $T_m \pm \Delta T$, and then swapped when the heat transfer rate reached an asymptotic value, at $t =$ 636 s. Observations reveal a slowdown in the heat transfer rate after 200 s, which prompts a recommendation to swap the endwall temperatures at this point in time. To implement this in practice, we propose rotating the PCM material inside the package while maintaining wall temperatures fixed. The suggested rotation concept has the potential to simplify the technological design of the system and facilitate its manipulation.

The strategy employed in case III was also applied to n-eicosane. As anticipated, this scenario yielded sufficiently good performance for n-eicosane. We expect that the suggested novel approach of PCM rotation will be supported by experimental evidence in future research. Note that unlike the previous case with *Ga*, the primary heat transfer mechanism for n-eicosane is Marangoni convection. The absence of the Marangoni effect would result in a heat transfer rate approximately 30 times weaker due to low thermal conductivity of n-eicosane. This finding could be be verified in future microgravtiy experiments.

CRediT authorship contribution statement

D. Dubert: Writing – original draft, Software, Methodology, Investigation, Formal analysis, Data curation. **B. Šeta:** Software, Investigation, Formal analysis, Writing – review & editing. **J. Massons:** Writing – original draft, Visualization, Methodology, Investigation, Formal analysis. **Jna. Gavaldà:** Writing – review & editing, Visualization, Software, Investigation, Funding acquisition. **M.M. Bou-Ali:** Writing – review & editing, Supervision, Investigation, Funding acquisition. **X. Ruiz:** Writing – original draft, Supervision, Software, Investigation, Funding acquisition, Conceptualization. **V. Shevtsova:** Writing – original draft, Supervision, Investigation, Conceptualization.

Declaration of competing interest

The authors declare that they have no known competing financial interests or personal relationships that could have appeared to influence the work reported in this paper.

Data availability

Data will be made available on request.

Acknowledgments

The work of M.M.B. and V.S. is supported by the Basque Government under the MMASINT project (KK-2023/00041 Elkartek programme) and Research Group Programme IT1505-22 and PID2020-115086GB-C33 financed by MCIN/AEI of the Spanish Government. The work of D.D., J.M., J.G, X.R. is supported by grants 2021PFRURV- 74 and 2022PFR-URV-12 (Rovira i Virgili University), AND PID2020-115086GB-C32 financed by (MICINN/FEDER) of the Spanish Government.

Appendix A. Supplementary data

Supplementary data to this article can be found online at https://doi.org/10.1016/j.icheatmasstransfer.2024.107741.

References

[1] J. Porter, A. Laverón-Simavilla, M. Bou-Ali, X. Ruiz, F. Gavaldà, J. Ezquerro, P. Salgado Sánchez, U. Martínez, D. Gligor, I. Tinao, J. Gómez, J. Fernández, J. Rodríguez, A. Borshchak Kachalov, V. Lapuerta, B. Šeta, J. Massons, D. Dubert, A. Sanjuan, V. Shevtsova, L. Garcia-Fernàndez, The effect of Marangoni convection on heat transfer in phase change materials experiment, Acta Astronaut. 210 (2023) 212–223.
[2] J. Collette, P. Rochus, R. Peyrou-Lauga, O. Pin, N. Nutal, M. Larnicol, J. Crahay, Phase change material device for spacecraft thermal control, in: In: 62nd International Astronautical Congress, Cape Town, South Africa, 2011 pp. IAC–11. C2.8.1.
[3] S. Morea, The lunar roving vehicle: Historical perspective, in: Proc. the Second Conference on Lunar Bases and Space Activities of the 21st Century, Houston, TX, USA, 5–7 April 1988 vol. 2, 1988, pp. 619–632.
[4] T.D. Swanson, G.C. Birur, Nasa thermal control technologies for robotic spacecraft, Appl. Therm. Eng. 23 (9) (2003) 1055–1065.
[5] T. Cichan, K. Timmons, K. Coderre, W. Pratt, The Orion Spacecraft as a Key Element in a Deep Space Gateway, Technical Lockheed Martin Paper, 2017, pp. 1–16.
[6] G. Quinn, T. Ahlstrom, H. Le, R. Sheth, Phase change material heat sink flight experiment results, in: 47th International Conference on Environmental Systems; Charleston, 2017, pp. 1–18.
[7] C. Vélez, M. Khayet, J. Ortiz de Zárate, Temperaturedependent thermal properties of solid/liquid phase change even-numbered n-alkanes: n-hexadecane, noctadecane and n-eicosane, Appl. Energy 143 (2015) 383–394.
[8] D.P. Colvin, J.C. Mulligan, Y.G. Bryant, Enhanced heat transport in environmental systems using microencapsulated phase change materials, SAE Trans. 101 (1992) 717–725.
[9] I. Garmendia, H. Vallejo, M. Seco, E. Anglada, Design and fabrication of a phase change material heat storage device for the thermal control of electronics components of space applications, Aerospace 9 (2022) 106.
[10] S. Madruga, C. Mendoza, Enhancement of heat transfer rate on phase change materials with thermocapillary flows, Europ. Phys. J. Spec. Top. 226 (2017) 1169–1176.
[11] J. Ezquerro, A. Bello, P. Salgado Sánchez, A. Laveron-Simavilla, V. Lapuerta, The thermocapillary effects in phase change materials in microgravity experiment: design, preparation and execution of a parabolic flight experiment, Acta Astronaut. 162 (2019) 185–196.
[12] J. Ezquerro, P. Salgado Sánchez, A. Bello, J. Rodríguez, V. Lapuerta, A. Laveron-Simavilla, Experimental evidence of thermocapillarity in phase change materials in microgravity: measuring the effect of marangoni convection in solid/liquid phase transitions, Int. Comm. Heat Mass Transf. 113 (2020) 104529.
[13] P. Salgado Sánchez, J.M. Ezquerro, J. Fernández, J. Rodríguez, Thermocapillary effects during the melting of phase-change materials in microgravity: steady and oscillatory flow regimes, J. Fluid Mech. 908 (2021) A20.
[14] P. Salgado Sánchez, J. Porter, J.M. Ezquerro, I. Tinao, A. Laverón-Simavilla, Pattern selection for thermocapillary flow in rectangular containers in microgravity, Phys. Rev. Fluids 7 (2022) 053502.
[15] N. García-Acosta, P. Salgado Sánchez, J. Jiménez, U. Martínez, J. Ezquerro, Thermocapillary-enhanced melting of different phase-change materials in microgravity, Microgravity Sci. Technol. 34 (2022) 92.
[16] R. Varas, U. Martínez, K. Olfe, P. Salgado Sánchez, J. Porter, J. Ezquerro, Thermocapillary and natural convection during the melting of pcms with a liquid bridge geometry, Microgravity Sci. Technol. 35 (2023) 17.
[17] B. Šeta, D. Dubert, J. Massons, J. Gavaldà, M.M. Bou-Ali, X. Ruiz, Effect of Marangoni induced instabilities on a melting bridge under microgravity conditions, Int. J. Heat Mass Transf. 179 (2021) 121665.
[18] B. Šeta, D. Dubert, M. Prats, J. Gavaldà, J. Massons, M. Bou-Ali, X. Ruiz, V. Shevtsova, Transitions between nonlinear regimes in melting and liquid bridges in microgravity, Int. J. Heat Mass Transf. 193 (2022) 122984.
[19] B. Šeta, D. Dubert, J. Gavaldà, J. Massons, M.M. Bou-Ali, X. Ruiz, V. Shevtsova, Effect of heat transfer through an interface on convective melting dynamics of phase change materials, J. Fluid Mech. 966 (2023) A46.
[20] B. Šeta, P. Salgado Sánchez, D. Dubert, J. Massons, J. Gavaldà, J. Porter, M.M. Bou-Ali, X. Ruiz, V. Shevtsova, Three-dimensional effects during thermocapillary-driven melting of PCMs in cuboidal containers in microgravity, Int. Comm. Heat Mass Transf. 150 (2024) 107198.
[21] S. Madruga, C. Mendoza, Scaling laws during melting driven by thermocapillarity, Int. J. Heat Mass Transf. 163 (2020) 120462.

[22] X. Chen, G. Hao, F. Yao, C. Zhang, Numerical study on melting phase change under microgravity, Microgravity Sci. Technol. 31 (2019) 793–803.
[23] H. Peng, W. Guo, M. Li, S. Feng, Melting behavior and heat transfer performance of gallium for spacecraft thermal energy storage application, Energy 228 (2021) 120575.
[24] X.-H. Yang, S.-C. Tan, J. Liu, Numerical investigation of the phase change process of low melting point metal, Int. J. Heat Mass Transf. 100 (2016) 899–907.
[25] S. Madruga, C. Mendoza, Introducing a new concept for enhanced micro-energy harvesting of thermal fluctuations through the Marangoni effect, Appl. Energy 306 (2022) 117966.
[26] H. Peng, W. Guo, S. Feng, Y. Shen, A novel thermoelectric energy harvester using gallium as phase change material for spacecraft power application, Appl. Energy 322 (2022) 119548.
[27] A.D. Brent, V.R. Voller, K.J. Reid, Enthalpyporosity technique for modeling convection-diffusion phase change: application to the melting of a pure metal, Num. Heat Transf. 13 (3) (1988) 297–318.
[28] F. Stella, M. Giangi, Melting of a pure metal on a vertical wall: numerical simulation, Num. Heat Transf. Part A: Appl. 38 (2) (2000) 193–208.
[29] N. Hannoun, V. Alexiades, T.Z. Mai, Resolving the controversy over tin and gallium melting in a rectangular cavity heated from the side, Numer. Heat Transf. B Fundam. 44 (3) (2003) 253–276.
[30] A. Sanjuan, B. Śeta, J. Gavaldà, X. Ruiz, V. Shevtsova, M. Bou-Ali, Comparative experimental-numerical analysis of pcm: n-hexadecane, n-octadecane and neicosane, in: 27th ELGRA Biennial Symposium & General Assembly. Lisbon (Portugal), 2022, pp. 68–69.
[31] P. Egolf, H. Manz, Theory and modeling of phase change materials with and without mushy regions, Int. J. Heat Mass Transf. 37 (18) (1994) 2917–2924.
[32] D.R. Poirier, Permeability for flow of interdendritic liquid in columnar-dendritic alloys, Metall. Trans. B 18 (1) (1987) 245–255.
[33] D. Dubert, B. Śeta, M. Simón, J. Gavaldà, J. Massons, A. Perez-Poch, X. Ruiz, The melting-solidification cycle for materials with different prandtl numbers, in: In Proc. 15th Int. Meeting of Thermodiffusion (IMT15), 2023, pp. 606–614.
[34] C. Gau, R. Viskanta, Melting and solidification of a pure metal on a vertical wall, J. Heat Transf. 108 (1) (1986) 174–181.